

Barkhausen noise in disordered strip-like ferromagnets: experiment vs. simulations

Djordje Spasojević and Miloš Marinković

Faculty of Physics, University of Belgrade, POB 44, 11001 Belgrade, Serbia

Dragutin Jovković

Faculty of Mining and Geology, University of Belgrade, POB 162, 11000 Belgrade, Serbia

Sanja Janičević

Faculty of Science, University of Kragujevac, POB 60, 34000 Kragujevac, Serbia

Lasse Laurson

Computational Physics Laboratory, Tampere University, POB 692, FI-33014 Tampere, Finland

Antonije Djordjević

*School of Electrical Engineering, University of Belgrade, 11000 Belgrade, Serbia and
Serbian Academy of Sciences and Arts, 11000 Belgrade, Serbia*

In this paper, we compare the results obtained from the low-frequency Barkhausen noise recordings performed on a VITROPERM 800 metallic glass sample with the results from the numerical simulations of the Random Field Ising Model systems. We show that when the values of disorder and driving rates of the model systems are suitably chosen, a considerable matching with the experimental results is achieved indicating that the model can reproduce a majority of the Barkhausen noise features.

I. INTRODUCTION

A multitude of systems respond to slowly changing external conditions by exhibiting a bursty, "crackling noise" type of response, consisting of a sequence of bursts of activity, or avalanches, characterized by scale-free power-law distributions [1]. A prime example of both fundamental and applied interest is given by Barkhausen noise (BN) [2]. It consists of irregular electromotive force (EMF) pulses induced by the jumps in magnetization caused by the jerky motion of magnetic domain walls in response to the slow changes of the external magnetic field.

The BN studies performed so far [3–20] have shown that the (individual) jumps, and therefore the BN pulses, are stochastic and that their distributions follow power laws described by power-law indices which satisfy certain scaling relations. Experimental studies of Barkhausen noise have been conducted both in bulk [8] and nonequilateral geometry samples, in particular thin films [9–11]. Two distinctive universality classes have been identified in polycrystalline and amorphous bulk materials, while in thin samples the question of universality remains to be resolved. The use of magneto-optical techniques [13] demonstrated the clear difference between the magnetic behavior of thin films and bulk materials, while more scrutinized investigations [16, 17, 19] confirmed the existence of various types of 2D dynamics in thin films with different thicknesses. BN is by no means unique in exhibiting crackling noise with power law statistics. Numerous other systems exhibit a similar pattern of behavior sharing the profound analogies despite fundamental differences in spatio-temporal scales, system geometry,

structure, underlying interactions and type of driving. Examples of such systems are covering a broad range from compressed nanocrystals [21], to imbibition fronts in porous materials [22], to plastic deformation due to collective dynamics of dislocations [23–26], heartbeat [27] and brain dynamics [28–30], earthquakes [31–33] to financial stock markets [34, 35].

Theoretical or numerical models of Barkhausen noise (BN) proposed in the literature include discrete spin models such as the Random Field Ising Model (RFIM) [36–39], micromagnetic simulations [40, 41], and various domain wall models describing domain walls as driven elastic interfaces in random media [42]. In this paper, we consider the non-equilibrium RFIM as a model system, and present a comparison of the simulation results with low-frequency BN recordings performed on a VITROPERM 800 metallic glass sample. We find that by tuning the disorder and driving rate parameters of the model appropriately, the model is able to reproduce most of the experimental BN features. Unlike in the equilibrium model version [43–46], in which the system evolves jumping between the equilibrium states determined by the current value of the external magnetic field, in the nonequilibrium model version, the system evolves through the nonequilibrium states following some local dynamic rule. The nonequilibrium version enables simulations of the time response of the system (mimicking BN) under all driving conditions and better corresponds to the BN experiments performed on metallic glasses which are by themselves not in equilibrium. Also, this model version is greatly computationally more efficient, so it enables simulations of much larger systems reducing the finite-size effects.

This paper is organized as follows: after the introduction in Section I, the details on the experimental analysis are presented in Section II, including Subsections II A and II B devoted to the description of the experimental setup and BN recordings. Section III showcases obtained results and contains Subsections III A and III B dedicated to the analysis of experimental BN response signals and hysteresis loops, a detailed explanation of the decomposition of BN signal into BN pulses, and experimental BN distributions, followed by Subsection III C devoted to the comparison of results of experimental BN measurements and numerical simulations of RFIM. The paper ends with discussion and conclusion presented in Section IV.

II. EXPERIMENTAL ANALYSIS

A. Experimental setup

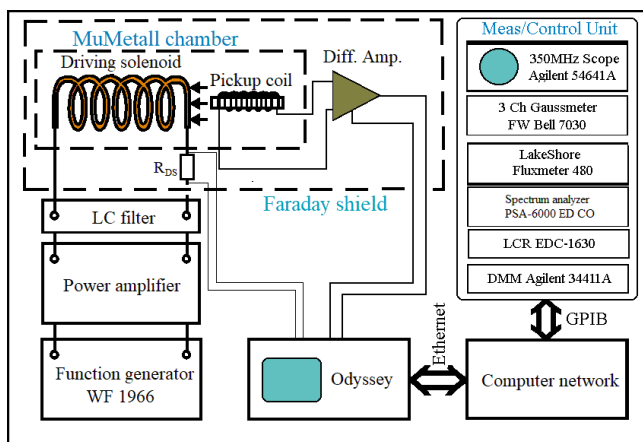


FIG. 1. Schematic presentation of the experimental setup used in our Barkhausen noise measurements.

We performed the Barkhausen noise recordings using the setup depicted in Fig. 1. The Barkhausen noise signal was collected by a pickup coil (1100 turns of AWG 34 copper wire 0.160 mm in diameter and 23.3 Ω resistance) tightly wound around the entire sample. The sample and the pickup coil were placed in the middle of a 30 cm long driving solenoid with a circular cross-section 5 cm in (inner) diameter, 840 turns in three rows of AWG 26 copper wire 0.405 mm in diameter and 5.7 Ω resistance. This driving coil provided the external magnetic field that is homogeneous along 80% of its axis with 1% tolerance due to the presence of two compensating coils (each with 50 turns of wire) placed at the driving coil ends.

The electric current, causing the external magnetic field by its flow through the driving coil, is produced at the output of a dedicated battery-operated transconductance amplifier from the input voltage signal generated by a function generator (two-channel Multifunction synthesizer WF 1966B, NF corporation, Japan, 0.01 μ Hz

- 50 MHz frequency range with ± 5 ppm accuracy, 14-bit waveform resolution and ± 10 V maximum output). The (digital high-frequency) generator voltage noise is suppressed at the amplifier input by a low-pass active filter (4 stages: Sallen-Key 20 Hz cutoff frequency, 12 dB/octave each, 48 dB/octave overall), so that the standard deviation of the generated current noise was less than 20 μ A providing driving virtually without digital and environmental noise.

The response signal (i.e. the electromotive force generated in the pickup coil) is routed from the pickup coil to a lab-made battery-operated two-stage voltage amplifier. In its first stage a CA-261F2 Low Noise Bipolar Amplifier (NF Corporation, Japan) is used with DC to 200 kHz frequency response, gain 40 dB \pm 0.2 dB, and equivalent input noise voltage of 0.8 nV/ $\sqrt{\text{Hz}}$. In the second amplifier stage a National Semiconductor LME 49720NA Dual High Performance, High Fidelity Audio Operational Amplifier is used with maximum gain 26.85 dB and equivalent input noise of 2.7 nV/ $\sqrt{\text{Hz}}$. The measurements were performed with the overall amplifier gain set at 2100, turned on a first-order RC filter in the feedback section of the amplifier with the cutoff frequency set to 160 kHz, and the overall equivalent input noise voltage less than 1 nV/ $\sqrt{\text{Hz}}$.

The amplified BN signal is led by a BNC cable to an OD200 acquisition card (four differential channels, 10 MHz/500 kHz maximum/continuous sampling rate on all channels, and 14-bit/16-bit resolution) of the Odyssey XE (Nicolet, USA) data acquisition system. Besides the BN signal, we also monitored on another OD200 channel the voltage at a $R_{DS} = 1.00 \Omega$ (metal film) resistor connected in series with the driving solenoid giving us, via the conversion factor of 2960 Am⁻¹/V, the time profile of the magnetic field H inside the driving solenoid.

The sample, pickup coil, and driving solenoid were enclosed in a cylindrical MuMetal chamber (Vacuum-schmelze, Germany) with four walls (each 3 mm thick) providing 50 cm high and 35 cm in diameter shielded volume, placed together with both amplifiers inside a sealed 1 m \times 1 m \times 1 m sound isolated Faraday shield made of 1 cm thick solid aluminium. Due to such shielding and battery-operated amplifiers, the recorded Barkhausen noise was virtually free from the external electromagnetic noise and pollution penetrating from the electric network, as well as from the external static/low frequency environment electric and magnetic field.

Let us also mention that in the calibration of the measurement system and for various types of control measurements we used 350 MHz oscilloscope Agilent 54641A, Three-channel Gaussmeter FW Bell 7030, LakeShore Fluxmeter 480, 6.2 GHz Spectrum analyzer PSA-6000 (EdCo, Korea), LCR meter EDC-1630 (EdCo, Korea), and Digital multimeter Agilent 34411A, whereas for the control of the ambiental electromagnetic noise and distribution of static voltage we used the TRIFIELD EMF Meter Model TF2 and Surface DC voltmeter SVM2 (AlphaLab, USA).

B. Barkhausen noise recordings

In this paper, we present the results of the BN measurements performed on a $16\text{ cm} \times 1\text{ cm} \times 40\text{ }\mu\text{m}$ sample of Vitroperm 800 supplied from Vacuumschmelze (VAC), Germany. Vitroperm 800 is a commercial nanocrystalline ferromagnetic alloy (82.8 Fe%, 1.3% Cu, 5.6% Nb, 8.8% Si, 1.5% B by weight) with crystal grains of diameter between approx. 10-15 nm surrounded by an amorphous residual phase. It has 1.24 T saturation magnetic polarization reached at the field strength above approx. 500 A/m, very high treatment-dependent initial susceptibility (up to 600 000), negligible magnetostriction, and 600 °C Curie temperature. This sample was annealed for 12 hours at 300 °C without a magnetic field.

The Barkhausen noise recordings were performed in the vertically oriented external magnetic field H parallel to the sample's longest side, which varied in time between -550 A/m and 550 A/m according to a periodic zero-mean triangle time profile at 0.5 mHz, 1 mHz, 2 mHz, 5 mHz, 10 mHz, 20 mHz, and 50 mHz frequency. For each frequency (0.5-10 mHz)/(20-50 mHz), the presented data are measured in the 10 V/20 V voltage span during 20 field cycles preceded by 50 cycles to reach a closed hysteresis loop. The measurements were performed in the continuous acquisition mode of the Odyssey XE data acquisition system at the 200 kS/s sampling rate with 16-bit resolution and turned on the internal anti-alias (low-pass) analog filter at 100 kHz cutoff frequency. The recorded data were stored in a 36 GB internal Odyssey XE acquisition SCSI hard disk, and after completion of measurements transferred to a hard disk of an external PC connected to Odyssey for the purpose of storage and numerical processing. All measurements were performed during weekend nights to minimize the amount of external (environmental and electric network) noise.

III. RESULTS

A. Experimental BN: response signal, hysteresis loops, and decomposition of BN signal into BN pulses

In Fig. 2 we illustrate the time profiles of the response signal and the external magnetic field recorded at 1 mHz driving frequency during one period. Examples of time profiles of response signals recorded in one half-period for each of the employed driving frequencies are shown in the main panels of Fig. 3, for (0.5 - 2 mHz)/(5 - 50 mHz) on the left/right main panel, together with the corresponding hysteresis loops presented in the right insets. Short excerpts of the response signal voltage, recorded around the maximum value of H when the sample is saturated, show in top-left insets the overall noise of the measurement system and the sample at $\Omega = 0.5\text{ mHz}$ (in the left main panel) and $\Omega = 50\text{ mHz}$ (in the right main panel). As illustrated by noise histograms in the bottom-left in-

sets, this noise is of the Gaussian type with a standard deviation of less than 5 mV at these two and likewise for the remaining frequencies, so the Signal-to-Noise-Ratio by amplitude was maintained above 1000.

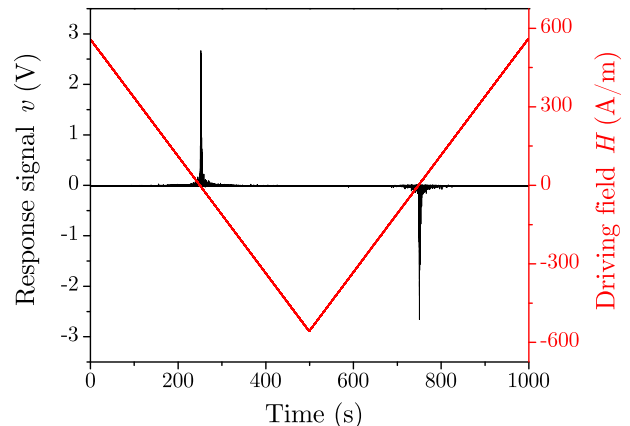


FIG. 2. Time profiles of the response voltage signal v (black line) and the external magnetic field H (red line) driving the sample at the 1 mHz frequency shown during one period. In our BN measurements, we connected the pickup coil so that the response signal had the polarity opposite to the sign of dH/dt .

As a part of the overall response signal, the pure BN signal arises due to the motion of the domain walls caused by flipping of magnetic moments tending to align with the local effective magnetic field. In ferromagnetic samples, this local field increases/decreases (almost everywhere) together with the external magnetic field, and therefore the corresponding values of induced electromotive force (EMF) are (almost always) one-sided. The domain wall motion proceeds in the form of one or several avalanches of finite duration possibly merging in time and space. Each such event induces a BN pulse - a sequence of nonzero pure BN signal values of the same sign realized in contiguous short intervals of time.

Fig. 4 shows a part of the recorded signal suggesting that the response signal can be considered as a train of BN pulses, separated in time by the inactivity intervals of the sample during which the pure BN signal is absent. This means that the recorded signal can be decomposed into BN pulses, which is, however, not straightforward due to the superimposed induced voltage caused not by the rearrangements of the magnetic domains, but by other means. Indeed, some EMF is induced in the pickup coil because of the varying external magnetic field even without inserted sample. For the noiseless triangle time profile of the driving field, this contribution would appear in the signal time profile as a horizontal line switching its level at the half-period transitions, whereas in reality some concomitant noise, caused by all factors except the change of sample's magnetization and therefore

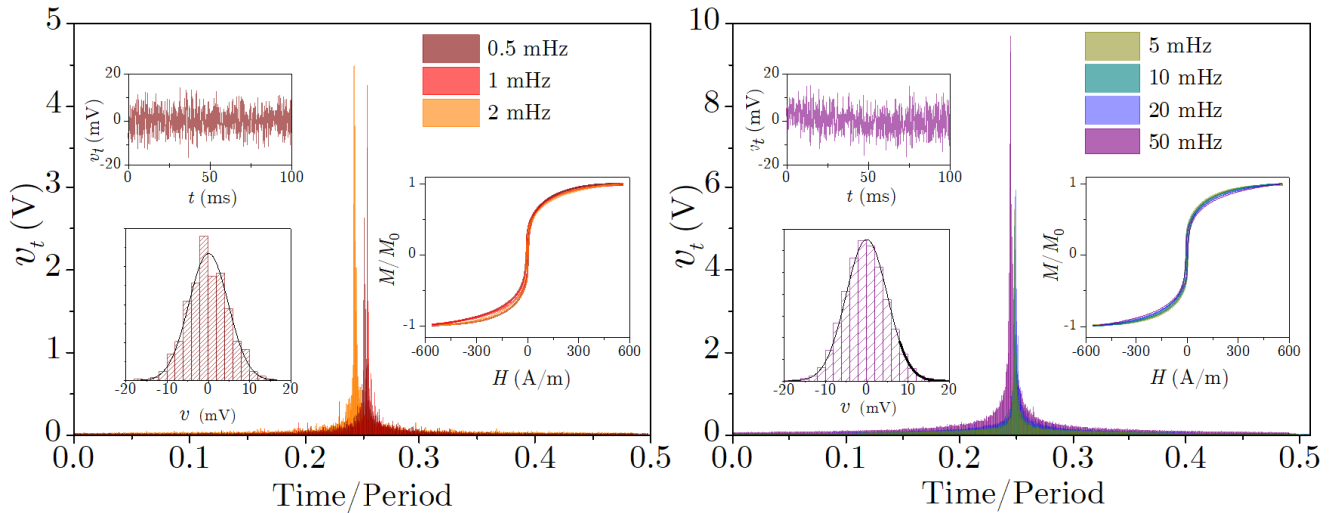


FIG. 3. Main panels show one example of time profiles of the voltage response signal v_t recorded during a single half-period of the external driving field H for each of the employed "slow" (left) and "fast" (right) driving frequencies Ω quoted in legends. Top-left inset in the left main panel presents an excerpt of the time profile of the response signal recorded at $\Omega = 0.5$ mHz near the maximum value of the external field H , while the histogram of presented values illustrates in the bottom-left inset of the same panel that these values are normally distributed, which could be mainly attributed to random fluctuations of sample's magnetization. In the right panel, the left insets show the same, but for $\Omega = 50$ mHz, while for the remaining frequencies, the corresponding distributions are roughly the same with the standard deviation less than 5 mV. Hysteresis curves, displaying versus the external magnetic field H the sample's magnetization M scaled by maximum magnetization M_0 , are given in the right insets.

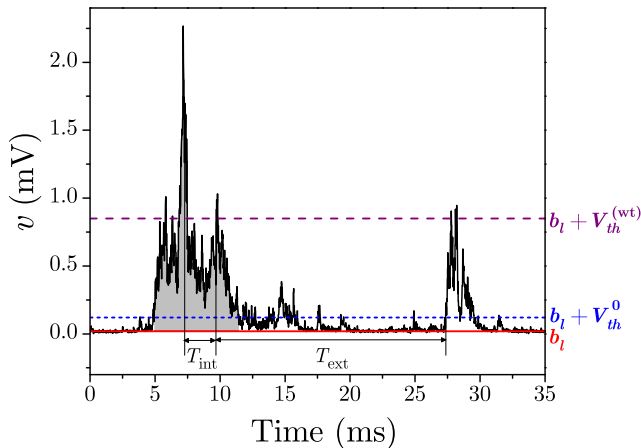


FIG. 4. Part of the time-profile of the response signal v (black line) and horizontal lines representing (bottom to top): the baseline b_l (red full line), base threshold level $b_l + V_{th}^0$ (blue dotted line), and waiting-time threshold level $b_l + V_{th}^{(wt)}$ (purple dashed line). Base threshold V_{th}^0 is used in the decomposition of the response signal into BN pulses (one such pulse is shaded in grey), while the waiting-time threshold $V_{th}^{(wt)}$ is used in the analysis of waiting times (e.g. internal and external waiting time, T_{int} and T_{ext}).

external, is inevitably superimposed as well. Due to this reason, several methods for baseline determination in the presence of noise (and investigated signal, here pure BN) have been proposed so far, see e.g. [47, 48]. Here, like in [4], we used the simplest and the fastest one in which the baseline level b_l is taken so that it corresponds to the discrete value of the digitized signal that is most frequently visited during the ongoing half-period, cf. Fig. 4.

The next step in the decomposition of the recorded signal into BN pulses is the establishment of some threshold region around the baseline and subsequent recognition of the recorded signal parts lying outside that region as BN pulses. Here, the threshold region is taken as the range of signal values v satisfying $b_l - V_{th} < v < b_l + V_{th}$ for some chosen threshold $V_{th} > 0$. As for the signal value v close to b_l one cannot resolve whether the external noise dominantly causes its part $v - b_l$ or not, the purpose of V_{th} is to discriminate between these two cases. So for $|v - b_l| < V_{th}$ (and small enough $V_{th} > 0$), one can consider that v is dominantly caused by other (i.e. non-BN) causes and disregard such signal points from further analysis of BN distributions, whereas the remaining part of the recorded signal, despite being polluted by the external noise, is taken as the BN signal relative to the baseline and proceeded to further analysis. For the threshold V_{th} used in the foregoing way we say that it plays the role of a *base* threshold, in which case we will denote it as V_{th}^0 .

The so-obtained BN signal is already decomposed into

BN pulses, each being a subsequence

$$\{v(t_s), v(t_s + \Delta t), \dots, v(t_e)\}$$

of the overall recorded sequence of digitized signal values $v(t)$ taken in the interval $\{t_s, t_s + \Delta t, \dots, t_e\}$ of contiguous discrete moments of acquisition time starting at t_s and ending at $n\Delta t$ later moment t_e , where Δt is the sampling interval ($= 5 \times 10^{-5}$ s in our case), cf. Fig. 3. t_s and t_e are defined in the usual way such that for a positive BN burst the signal goes above the threshold at $t = t_s$ and stays above the threshold until $t = t_e$, when it goes below the threshold for the first time after the start of the burst; note that for negative bursts, the opposite applies (i.e., the event starts at $t = t_s$, when the signal goes below the negative threshold and lasts until it goes above it at $t = t_s$). Each BN pulse of a ferromagnetic sample is either positive or negative, i.e. all its values are either above $b_l + V_{\text{th}}^0$ or below $b_l - V_{\text{th}}^0$, depending on the sign of dH/dt , cf. Fig. 2.

The collection of BN pulses extracted via the foregoing procedure from the overall recorded signal depends on the choice of threshold V_{th} . Because the basic role of imposing a threshold is to keep in further analysis most of the data points that are likely caused by BN reasons, a natural way would be to choose a threshold taking into account the width w of the external noise. As explained in [4], this width can be estimated from the data lying below the baseline and take V_{th}^0 proportional to this width, $V_{\text{th}}^0 = d_l w$, using reasonable discrimination levels d_l (e.g. between 0.5 and 3). Alternatively, the base threshold can be chosen differently, e.g. fixed to some constant value approximately matching the width of external noise, as we did in this paper.

Besides playing the role of a base threshold that is used in the decomposition of the response signal into BN pulses, variable threshold values are used in the analysis of waiting times (see the next subsection) in which case such threshold will be referred to as the waiting-time threshold $V_{\text{th}}^{(\text{wt})}$. The logic here is to first define a pulse with one threshold (V_{th}^0), and then a new threshold with another value ($V_{\text{th}}^{(\text{wt})}$) in order to be able to classify the waiting times into internal (due to breaking of the bursts into sub-avalanches) and external ones (those separating the "original" bursts) [49].

B. Experimental BN distributions

Each BN pulse $\{v(t_s), v(t_s + \Delta t), \dots, v(t_e)\}$ is characterized by several parameters. Mostly analyzed are its size

$$S = \sum_{k=0}^n [v(t_s + k\Delta t) - b_l] \Delta t,$$

duration

$$T = t_e - t_s,$$

i.e. the time interval between its ending moment t_e and starting moment t_s , energy

$$E = \sum_{k=0}^n [v(t_s + k\Delta t) - b_l]^2 \Delta t,$$

and amplitude

$$A = \max\{v(t_s) - b_l, \dots, v(t_e) - b_l\}.$$

Regarding the question of to what extent are the so-obtained parameter values affected by the external noise, one can take that while the width of (zero-mean) noise is comparatively small and its values uncorrelated, it can not affect much the individual parameter values for moderate and large BN pulses, and likely has no effect on their statistics.

In Fig. 5 are presented the log-log plots of the experimental probability density functions (i.e. distributions with the unit area at the lin-lin scale) of size S , duration T , energy E , and amplitude A of BN pulses extracted along the entire hysteresis loop at six values of base threshold V_{th}^0 from the signals recorded at 5 mHz. Previous studies of Barkhausen noise emissions (see e.g. [4, 50]) and our data from Fig. 5 show that these distributions follow the (modified) power-laws

$$D_X(X) = \mathfrak{D}_X(X/X_0, X/X_1, \dots) / X^{a_X}, \quad (1)$$

where X stands for one of the avalanche parameters (size S , duration T , energy E , and amplitude A), and a_X for the pertaining power-law exponent (τ , α , ε and μ for $X = S, T, E, A$, respectively). The exponents are associated with the slope of the log-log plot of $D_X(X)$ in its scaling region (i.e. the part in which this plot appears as linear), while the cutoff function $\mathfrak{D}_X(X/X_0, X/X_1, \dots)$, depending on the cutoff parameters X_0, X_1, \dots , describes the departure of $D_X(X)$ from the power law shape at the distribution ends (e.g. $\mathfrak{D}_X(X/X_l, X/X_u) \approx \text{const}$ for $X_l \leq X \leq X_u$ for the cutoff function specified by the lower cutoff X_l and the upper cutoff X_u).

The data displayed in Fig. 5 show that, although the choice of base threshold affects the shape of distributions, they all exhibit scaling regions which seem to be visually approximately parallel in their main part. This we quantified by extracting the effective values of the corresponding exponents (by the simple linear fit applied in the main part of the scaling region for each of them; see the comment [51]) and presenting their variation with the chosen base threshold V_{th}^0 in the inset for each of the distributions. Except for the energy exponent ε , the so-obtained exponent values are not constant, but instead show a systematic change with V_{th}^0 maintaining (within the uncertainty bars) the fulfillment of the scaling relations [4, 52, 53]:

$$\tau = 1 + (\alpha - 1) / \gamma_{S/T} \quad (2)$$

$$\varepsilon = 1 + (\alpha - 1) / (2\gamma_{S/T} - 1) \quad (3)$$

$$\mu = 1 + (\tau - 1) / (1 - 1/\gamma_{S/T}) \quad (4)$$

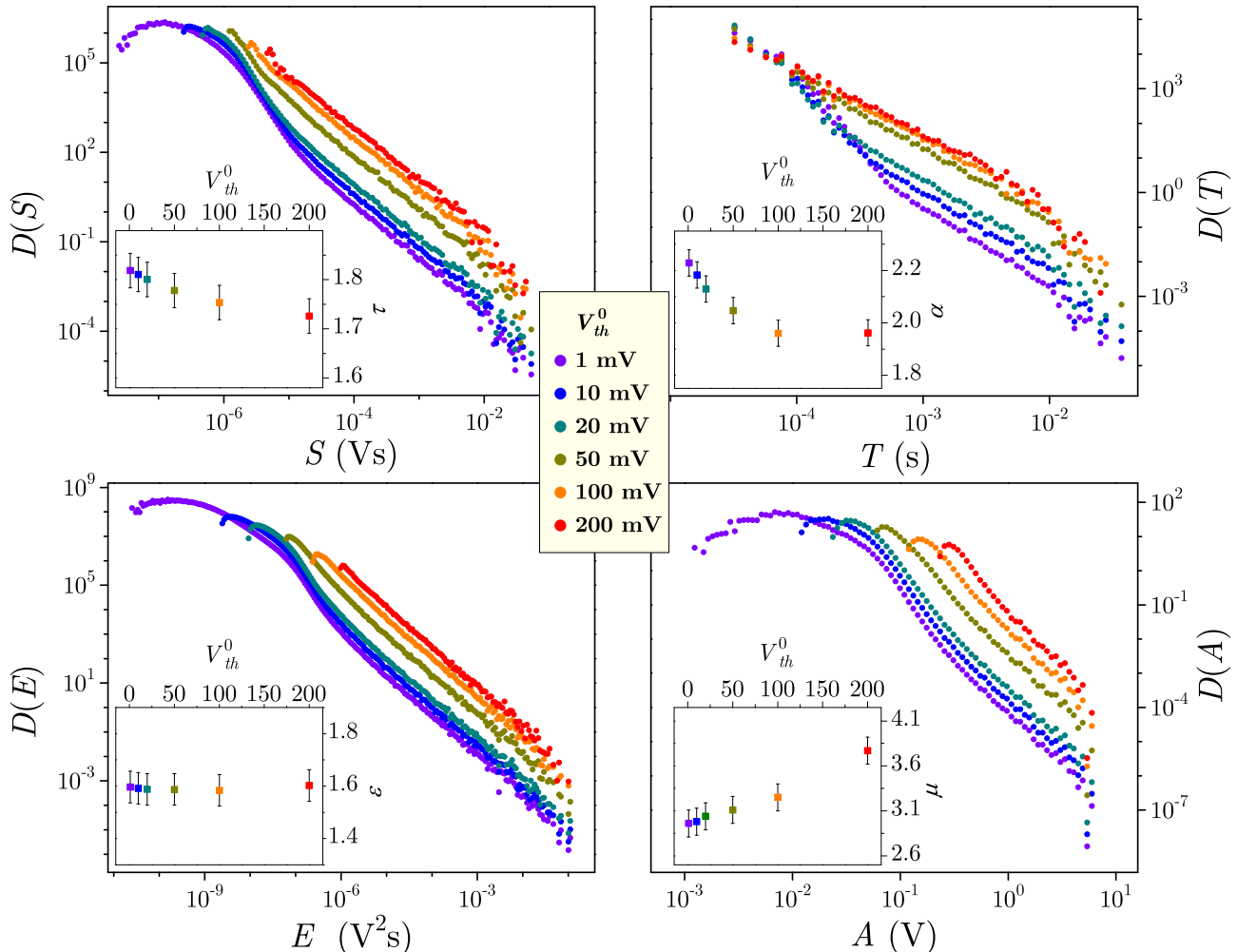


FIG. 5. For the values of base threshold V_{th}^0 quoted in the (common) legend, we give in main panels the integrated distributions of size S , duration T , energy E , and amplitude A of BN pulses all collected from the data recorded in 20 cycles of the external magnetic field at the same driving rate $\Omega = 5$ mHz. All distributions are normalized to the unit area at the lin-lin scale so as to be the experimental probability density functions. In the insets, we show the variation with V_{th}^0 of the effective values of the distributions' exponents (τ for $D(S)$, α for $D(T)$, ε for $D(E)$, and μ for $D(A)$) with the error bars mainly caused by the variation of the fitting region.

containing the exponent $\gamma_{S/T}$, see (5), whose variation with V_{th}^0 is shown in the left panel of Fig. 9.

Regarding the choice of the base threshold values employed in Fig. 5, we notice that, due to 5 mV noise width, the value of 1 mV base threshold is too small, enabling some signal parts dominated by the external noise to be recognized as (small) BN pulses, and also an occasional artificial merging of several separate BN pulses lined up in a sequence into larger ones. The next two values of V_{th}^0 , namely 10 mV and 20 mV, should be the most appropriate at the current (i.e. 5 mV) noise width because they statistically eliminate the influence of external noise and do not discriminate recognition of BN pulses that are

not too small. The distributions extracted at these two V_{th}^0 values indicate the existence of two scaling regions like the ones observed in the case of the RFIM avalanche distributions of thin systems, see [54–57]. There it was shown that the small avalanches, not reaching the system borders, propagate like in bulky 3D systems, whereas the big avalanches effectively propagate like 2D avalanches being sandwiched between the top and bottom system boundaries. So, the small 3D-like avalanches dominate in the initial steeper scaling region, followed by the less steep one caused by the big 2D-like avalanches. The initial (i.e. 3D-like and steeper) part of the distributions' scaling region gradually vanishes with further increase

of V_{th}^0 and the distributions attain the shape of a single-slope power law sharply decreasing at the large avalanche end.

Experimental BN studies performed so far revealed that between the duration T and the average size $\langle S \rangle_T$ of BN pulses of duration T should exist the correlation of a power-law type

$$\langle S \rangle_T \sim T^{\gamma_{S/T}}, \quad (5)$$

specified by the power-law exponent $\gamma_{S/T}$. Our 5 mHz data from the top panel of Fig. 6 suggest that the experimental value of this exponent, determined from the slope of the scaling region in its large-avalanche (linear) part, slightly depends on the choice of base threshold as is visible in the figure. Moreover, our data for $V_{\text{th}}^0 < 50$ mV indicate the presence of two scaling parts in graphs. The initial one shows the correlations between $\langle S \rangle_T$ and T for small avalanches and continues through a transitional region to the main part of the scaling region giving the correlations for larger avalanches.

The BN power spectrum $P(f)$, i.e. the (spectral) density of power released by the BN signal at frequency f , is expected to follow the power law

$$P(f) \sim f^{-\gamma_{\text{spc}}}, \quad (6)$$

specified by the power exponent γ_{spc} . In experiments, the BN signal is polluted by the external noise, so that the experimental power spectrum deviates from the power law most notably at the higher frequencies at which the noise dominates the Fourier components of the BN signal. This is noticeable in the experimental power spectra, exemplified in the bottom panel of Fig. 6 by the integral spectra recorded at three driving rates (0.5 mHz, 5 mHz, and 50 mHz) along the entire hysteresis loop (and shown by the pale lines). The clearest example is the 0.5 mHz integral spectrum whose power-law part is absent due to the proportionally longest interval of time virtually without the BN noise. As the driving rate increases, the interval with a pronounced BN signal gets proportionally longer so does the power-law spectrum part. To reduce the influence of noise, we also calculated the binned power spectra, i.e. the power spectrum of the response signal recorded in a narrow window of the external magnetic field centered at that value of H at which the averaged response signal attains its maximum. Under our experimental conditions, the binned spectra seem to be only weakly polluted by the external noise up ~ 20 kHz, so their power-law part extends that far.

As previously mentioned, thresholds are also used in the analysis of waiting times which are defined in the following way. For any threshold $V_{\text{th}}^{(\text{wt})}$, chosen for the waiting-time analysis, some parts of the response signal remain below the imposed waiting-time threshold level $b_l + V_{\text{th}}^{(\text{wt})}$, meaning that at any moment t in such part $v(t) < b_l + V_{\text{th}}^{(\text{wt})}$. The start t_s and end t_e of each of the corresponding intervals of time are (figuratively speaking) determined by two successive intersections of the

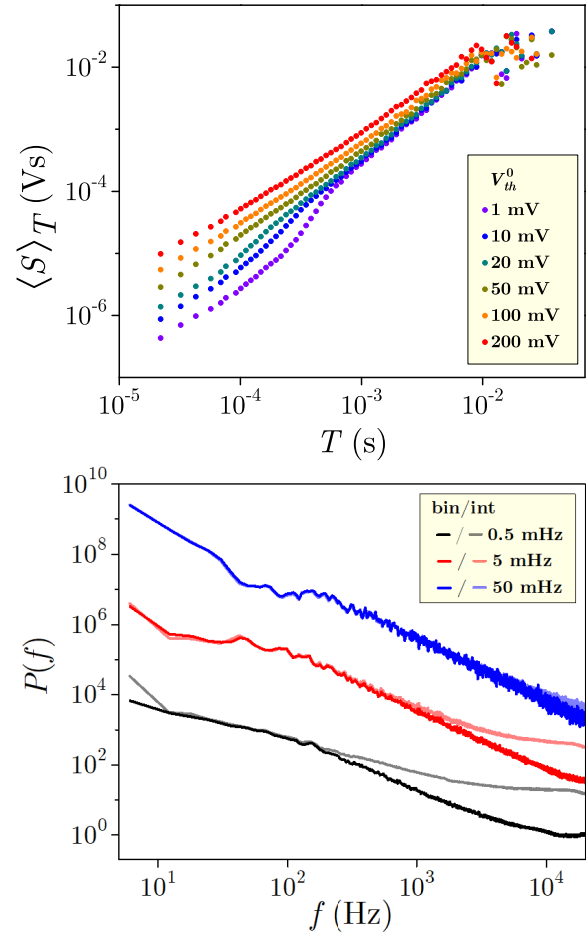


FIG. 6. Top panel: correlations between duration T and the average size $\langle S \rangle_T$ of BN pulses with duration T obtained for the same values of base threshold V_{th}^0 as in Fig. 5. Bottom panel: BN power spectra $P(f)$ against frequency f collected at three driving rates (0.5 mHz, 5 mHz, and 50 mHz) along the entire hysteresis loop (int) and in a narrow window (bin) of the external magnetic field centered at the maximum of the average response signal. For both panels, the underlying sets of experimental data are the same as in Fig. 5.

response signal with the waiting-time threshold level, see in Fig. 4. So, one can take the duration $T_w = t_e - t_s$ between these two moments t_s and t_e as the *waiting time*, and classify it either as the *external* waiting time T_{ext} or *internal* waiting time T_{int} if the moments t_s and t_e belong to different/same activity event, respectively.

In Fig. 7, we present three types of distributions of waiting time: total waiting time T_w in the top panel, external waiting time T_{ext} in the middle panel, and internal waiting time T_{int} in the bottom panel. These distributions become of a power-law type for the sufficiently high values of waiting-time threshold $V_{\text{th}}^{(\text{wt})}$ signifying the presence of temporal correlations; otherwise, they are ex-

ponential, showcasing the random waiting times and absence of temporal correlations.

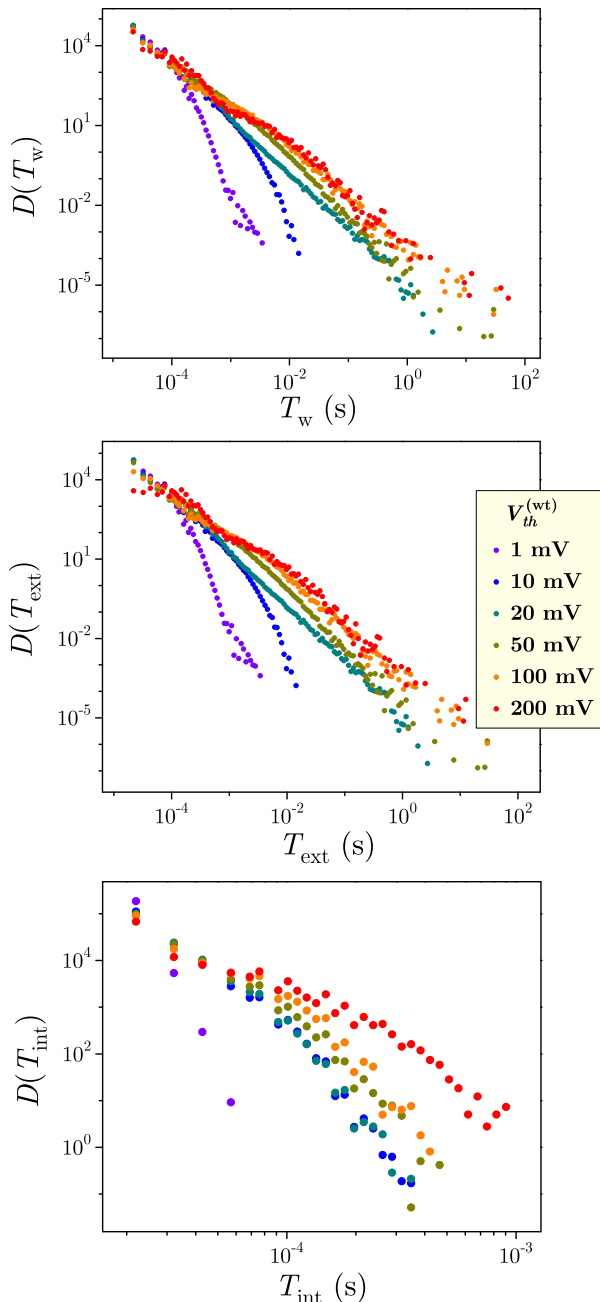


FIG. 7. Distributions of various types of waiting times: total T_w in the top, external T_{ext} in the middle, and internal T_w in the bottom panel. The distributions are obtained at the 5 mHz driving frequency for the same threshold levels and the same sets of data as in Fig. 5.

C. Comparison with RFIM

In this section, we compare our experimental results with the results of numerical simulations of the athermal nonequilibrium Random Field Ising Model [36, 39] driven at finite rates with the aim to test its suitability for interpretation of the behavior of field-driven disordered ferromagnets. Since at room temperature conditions, like in our experiment, thermal fluctuations in real systems should not be important, we employed the athermal (i.e. zero-temperature) model version [37–39] which is significantly less demanding than the thermal (i.e., finite-temperature) version. In the athermal version the distribution of the random field is quenched and therefore the model behavior is fully deterministic, meaning that driving the system through the next hysteresis cycle gives the same results. This is not consistent with BN experiments having a somewhat different response in repeated hysteresis cycles that might originate, e.g., from thermal noise and/or redistribution of stress within the sample from cycle to cycle. To overcome this deficiency, simulations are performed using a different configuration of the random field in each run, and the so obtained results are averaged over employed configurations having all the same value of the disorder parameter (this is known as quenched averaging).

1. On the model and numerical simulations

In the Random Field Ising Model, the Ising spins $s_i = \pm 1$, located at the sites i of a lattice, interact with their nearest neighbors ferromagnetically, and are exposed to a time-varying homogeneous external magnetic field H and a quenched random magnetic field taking uncorrelated values h_i from a zero-centered Gaussian distribution with the standard deviation R measuring disorder in the system.

The spin s_i is stable at the moment t_m of model time if $h_i^{\text{eff}}(t_m)s_i \geq 0$, where

$$h_i^{\text{eff}}(t_m) = \sum_j s_j^{(i)} + H(t_m) + h_i, \quad (7)$$

is the effective field acting on s_i at the moment t_m encompassing the influence of its nearest neighbors $s_j^{(i)}$ and the external field H (both taken at that moment t_m), and the random field h_i at its site; otherwise, s_i is unstable, and all unstable spins will flip reducing the value of the system Hamiltonian

$$\mathcal{H} = - \sum_{\langle ij \rangle} s_i s_j - H \sum_i s_i - \sum_i h_i s_i, \quad (8)$$

at the next moment $t_m + \Delta t_m$ of the (discrete) model time with $\Delta t_m = 1$. Such spin-flipping spreads like an avalanche until all spins in the system become stable.

In the adiabatic regime [39, 58] each avalanche is nucleated due to such change in the external magnetic field H that destabilizes only the least stable spin; thereafter, H is kept constant as long as the nucleated avalanche lasts propagating over the shell of the nearest neighbors of spins flipped at the previous moment, the shell being placed at the rim of the cluster of spins flipped during the ongoing avalanche.

On the other hand, in the finite rate driving regime, the incessant change of the external magnetic field facilitates the propagation of the ongoing avalanche(s) and occasionally causes the nucleation of new ones [59–62]. This leads to the overlapping in time of such separately nucleated avalanches and possibly their merging in space forming a single activity event [63]. The activity events are separated in time by the intervals of the system's inactivity, leading in this model version to the natural choice of baseline level $b_l = 0$ and identification of the event parameters (size S , duration T , energy E , and amplitude A) like in the experimental case, but after setting the value of base threshold in simulations to $V_{th}^0 = 1$.

Because of the symmetry between the rising and falling part of the hysteresis loop, we performed the numerical RFIM simulations only along the rising part by the field $H(t)$ increasing at some driving rate $\Omega = \Delta H / \Delta t_m$ which was constant like in our experiments. Each simulation starts with all spins set to -1 and some concordant big negative value of H , and afterward H is increased until all the spins are flipped to 1. We performed the simulations with the aid of the so-called sorted list algorithm (see in [52, 64]) modified and adjusted for the finite-rate driving regime.

2. Comparison of results of experimental BN measurements and numerical simulations of RFIM

In order to optimally match the simulation results to experimental, one can adjust in simulations the shape and size of the lattice, the value of disorder R , and the value of driving rate Ω . To this end, we performed simulations using the 32768 x 2048 x 8 strip-like cubic lattice with open boundaries mimicking our experimental samples by the ratio of its sides.

Next, because of unknown value of disorder which might provide results similar to the experimental, we performed simulations for several values representing all three domains of disorder for the employed lattice (below critical, transitional, and above critical, see in [58]), and for each of them at a set of values of Ω from 10^{-10} to 10^{-6} covering for this lattice all types of driving regimes from slow (without spanning events [65, 66]) to fast (large spanning events of quasi-2D type [67]), see in [61, 63].

For each pair of simulation parameters (R, Ω) we performed 20 simulations with different realizations of the random magnetic field. As the activity events in simulations are clearly extraditable as the longest subsequences of the non-zero values appearing in the (noiseless) re-

sponse signal at contiguous moments of time, the collecting of their statistics would be natural to perform with the base threshold $V_{th}^0 = 1$. Still, for the intended comparison with experiments, we did this for all distributions at the same base threshold $V_{th}^{sim} = 5$ in simulations and at the same base threshold in experiments $V_{th}^{exp} = 50$ mV. Despite the ($V_{th}^{exp}, V_{th}^{sim}$) pairs, chosen individually for each pair of the compared distributions, would provide closer matching, for simplicity we decided to perform all comparisons using the above pair of fixed thresholds with a remark that at and above $V_{th}^{exp} = 50$ mV the $\langle S \rangle_T - T$ experimental correlations have the scaling region with a single slope, c.f. Fig. 6, and that for $V_{th}^{sim} = 5$ and all employed rates the ratio (RMS of simulation signal)/ V_{th}^{sim} is roughly the same as in experiment at $V_{th}^{exp} = 50$ mV.

In Fig. 8 we compare the integrated distributions of avalanche event parameters (size, duration, energy and amplitude) collected in our experimental measurements and in numerical simulations. The presented simulation distributions are obtained for disorder $R = 2.3$, being above the effective critical disorder for the adiabatically driven 32768 x 2048 x 8 RFIM system [57], and at a set of "nice" values of the driving rate quoted in legend chosen in the same progression as the experimental ones. Among the tested driving rates and disorder values, ranging between $R = 1.8$ and $R = 3.0$ in 0.1 increments, this combination of driving rates and disorder provided the best achieved matching between experimental and simulation distributions presented in this and all subsequent figures.

Because of the different time and signal scales in the experiment and in simulations (real scales in the experiment, and discrete model scales in simulations), the matching of the two is achieved by dividing the simulation time scale by the factor $c_t = 2 \times 10^5$ (equal to the sampling rate used in our experiment) and the signal scale by the factor $c_v = 50$ (hence, the factor $c_t c_v = 10^7$ for the scale of avalanche size and the factor $c_t c_v^2 = 5 \times 10^8$ for the scale of avalanche energy) providing the best matching with the experimental distributions. In addition to this, due to the existing difference in both the shape and the logarithmic span, the distributions obtained from the simulations are shifted along the vertical axis so to attain the best overlapping in the scaling regions of the pairing distributions obtained in the experiment.

The data presented in Fig. 8 show a significant overlapping for the pairs of distributions at faster rates and overlapping in the scaling region, but noticeable discrepancies in the initial and final part of the distributions at slower rates. The overlapping is the least in the case of amplitude distributions which could be related to a significantly smaller dynamic range of the simulated response signal at the chosen lattice size.

Comparison between the experimental and simulation $\langle S \rangle_T - T$ correlations, presented in the left panel of Fig. 9, is performed for the same sets of experimental and simulation data as in Fig. 8 using the same

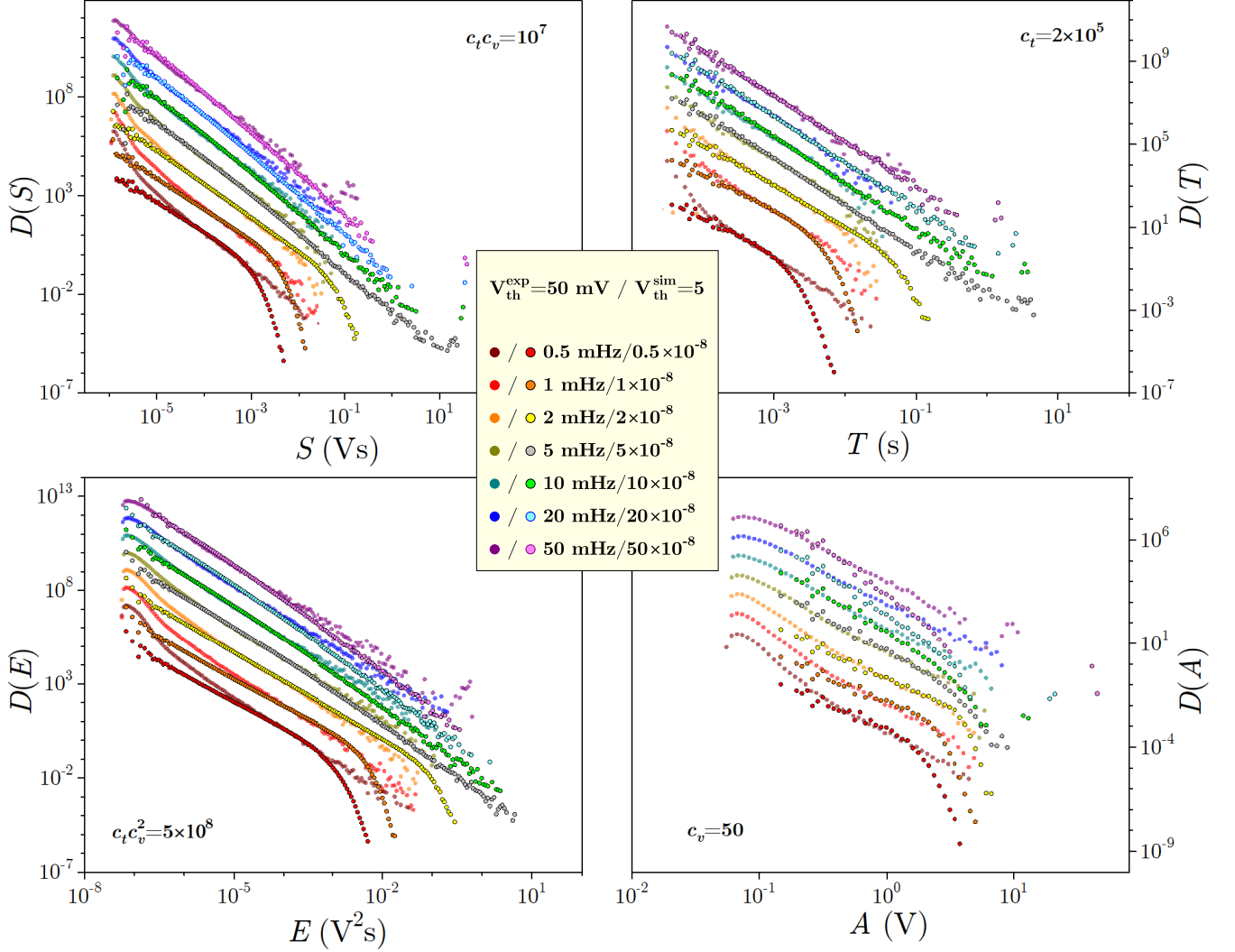


FIG. 8. Comparison of integrated (unit area) distributions of avalanche parameters (size S , duration T , energy E , and amplitude A) obtained in experiments and numerical RFIM simulations for the experimental/simulational driving rates quoted in the common legend. Each experimental distribution is extracted at the (same) experimental base threshold $V_{\text{th}}^{\text{exp}} = 50$ mV out of 20 hysteresis cycles data and presented with full symbols on the requisite scale using SI units for time and voltage. Starting from the distribution recorded at the lowest driving rate, each experimental distribution obtained at the next (higher) rate is for better visibility vertically translated by one decade upwards relative to the distribution recorded at the previous (lower) rate. Each simulational distribution is extracted at the (same) simulational base threshold $V_{\text{th}}^{\text{sim}} = 5$ out of 20 RFIM simulations on the $32768 \times 2048 \times 8$ cubic lattice performed with different realizations of the random magnetic field with disorder $R = 2.3$. For comparison, the simulational distributions, presented by empty symbols, are shifted along the horizontal axis dividing the data by a suitable factor ($c_t = 2 \times 10^5$ for T -axis, $c_v = 50$ for A -axis, $c_t c_v = 1 \times 10^5$ for S -axis, and $c_t c_v^2 = 5 \times 10^8$ for E -axis).

c_t and $c_t c_v$ factors and the same threshold pairs. The best overlapping is obtained between 1 mHz/ 1×10^{-8} and 2 mHz/ 2×10^{-8} experimental/simulational driving rates, while for higher rates the experimental correlations depart more and more from the power law, likely due to spatial merging of avalanches occurring at these rates.

Even more intricate is the behavior of power spectra. Comparison of the experimental and simulational binned spectra for the used experimental/simulational driving

rates is shown in the right panel of Fig. 9. The compared data suggest that the experimental BN (binned) spectra can be described by the power law

$$P(f) \sim f^{-\gamma_{S/T}}, \quad (9)$$

meaning that the power exponents γ_{spc} and $\gamma_{S/T}$ might be the same, as it was suggested in [68] within the RFIM context. Here, however, one must take into account that both experimental and simulational effective values of the

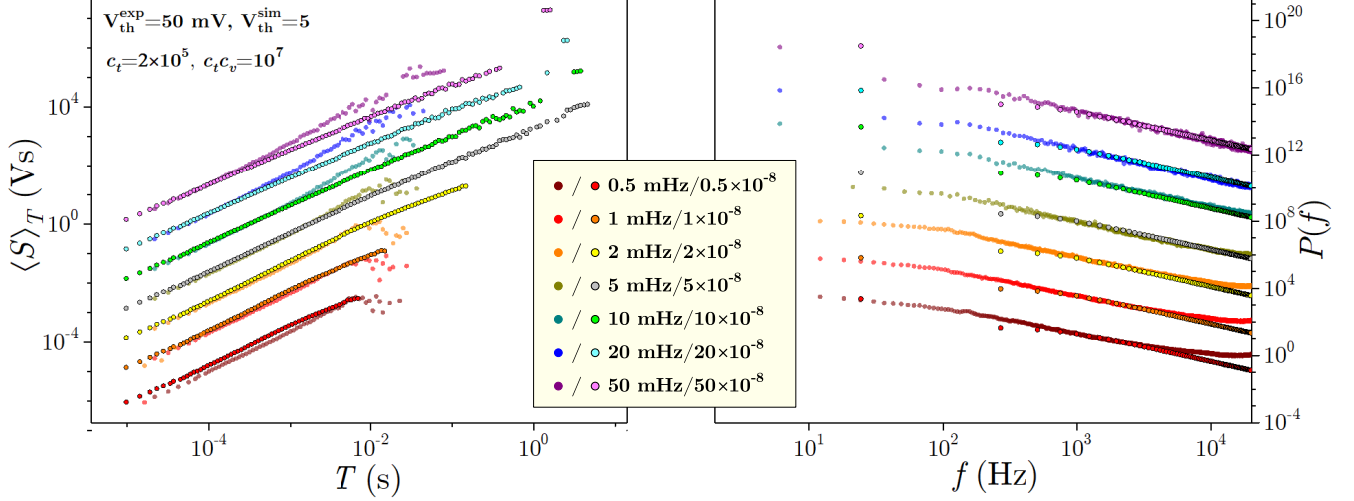


FIG. 9. Left panel: comparison of the experimental and simulational correlations between the avalanche duration T and the average avalanche size $\langle S \rangle_T$ of that duration extracted at the same experimental and simulational base thresholds, the same values of experimental and simulational driving rates, and the same c_t and $c_t c_v$ factors as in Fig. 8. Right panel: comparison of the experimental and simulational power spectra $P(f)$ for the driving rates from the legend. Simulational frequencies are multiplied by the factor $c_t = 2 \times 10^5$. For visibility, each of the next-driving-rate curves in both panels is shifted vertically upwards by one/two decades in left/right panel relative to the previous one. The underlying sets of data are the same as in Fig. 8.

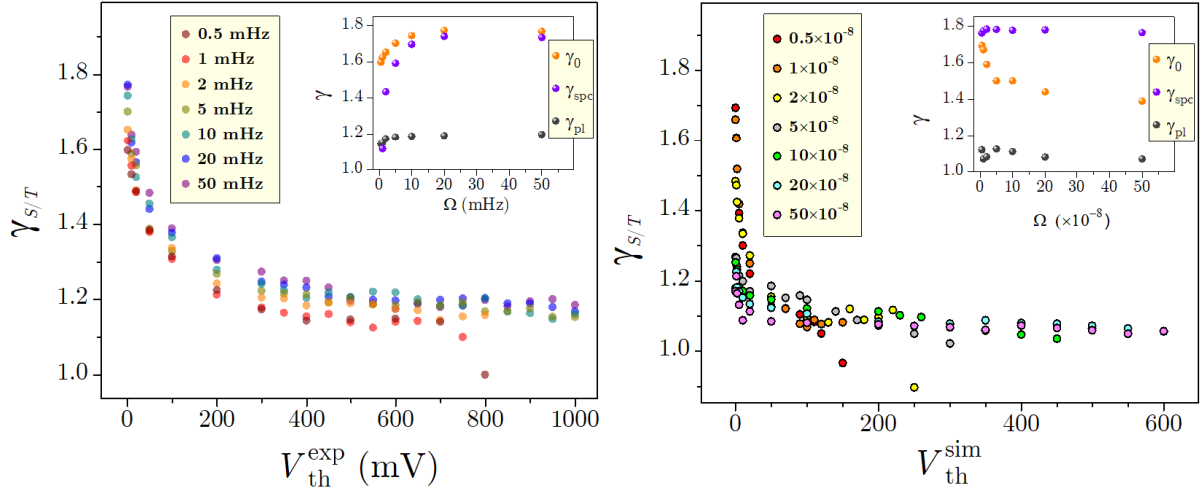


FIG. 10. Left panel: effective experimental values of the exponent $\gamma_{S/T}$ against the base threshold V_{th}^{exp} . In the inset, we show against the driving rate Ω the effective experimental values of γ_0 (i.e. the value of $\gamma_{S/T}$ at the current driving rate Ω for the smallest experimental base threshold $V_{th}^{exp} = 1$ mV), γ_{spc} (i.e. power spectrum exponent), and γ_{pl} (i.e. plateau value of the exponent $\gamma_{S/T}$ at the corresponding driving rate Ω). Right panel: the same as in the left panel, but for the values obtained from the simulational data. Each effective exponent value is the slope determined by the linear fit in the power law region of the corresponding distribution. The underlying data sets and other relevant parameters are the same as in Fig. 8.

exponent $\gamma_{S/T}$ depend on the choice of the imposed base threshold V_{th}^0 and on the driving rate Ω , which we illustrated in Fig. 10. The data displayed in this figure show that both γ_{spc} and $\gamma_{S/T}$ vary with threshold V_{th}^0 in a similar way decreasing from their maximum values at zero base threshold towards values at a plateau, one in the experimental and the other (~ 0.1 lower) in the simulational case, attained at rather high base thresholds. For each fixed value of base threshold V_{th}^0 , the variation of $\gamma_{S/T}$ with Ω is less, but present, including the plateau values. On the other hand, the effective values of γ_{spc} for different Ω , displayed in the insets of these main panels, seem to be the same in the experimental case as the corresponding values of γ_0 (i.e. the effective value of $\gamma_{S/T}$ for the smallest base threshold V_{th}^0 at the current driving rate Ω), but not in the simulational case except for the very small driving rates. However, in both experimental and simulational cases, the power exponent γ_{spc} is undoubtedly different for the corresponding plateau values at all driving rates.

In Fig. 11 we compare the distributions of waiting time: total, external, and internal shown in the top, middle, and bottom panel, respectively. The distributions calculated from the experimental and simulated data are overlapped to a high degree in the whole range of waiting times, except for the distributions of internal waiting times which overlap only in their scaling regions.

The average avalanche shape [70] is given by $\langle v_t/v_t^{\max} \rangle$ (i.e. the average value of the response signal v_t scaled by its maximum value v_t^{\max} during the avalanche) taken as a function of t/T (i.e. the time t measured from the beginning of avalanche scaled by the avalanche duration T). Fig. 12 shows that both in experiment and simulations these shapes are parabolic-like and rather similar, the experimental being slightly right-skewed and simulational (even less) left-skewed. Performing the fits of the average avalanche shape data to the functional form (found in [70])

$$\langle V(t|T) \rangle \propto T^{\gamma-1} \left[\frac{t}{T} \left(1 - \frac{t}{T} \right) \right]^{\gamma-1} \left[1 - a \left(\frac{t}{T} - \frac{1}{2} \right) \right] \quad (10)$$

allows us to estimate exponent γ as the fitting parameter; here parameter a accounts for the underlying asymmetry of the average avalanche shape. So-estimated values of γ are contrasted to the $\gamma_{S/T}$ data and are shown in the inset of Fig.12 against the driving rate Ω . One can observe that the values remain fairly close and consistent in the region of low driving rates, but begin to vary more and more as the driving rate increases. Two of the representative fits to the function (10) are included in the main panel of Fig. 12, shown with full line.

Finally, in Fig. 13 we contrast the magnetizations and magnetic susceptibilities obtained from the experiment and the numerical simulations. Magnetizations, rescaled by the saturation value M_0 and susceptibilities dM/dH , are presented against the external magnetic field H . Regarding the behavior of these curves below and above the coercive field H_c (i.e. the value of the external field H at

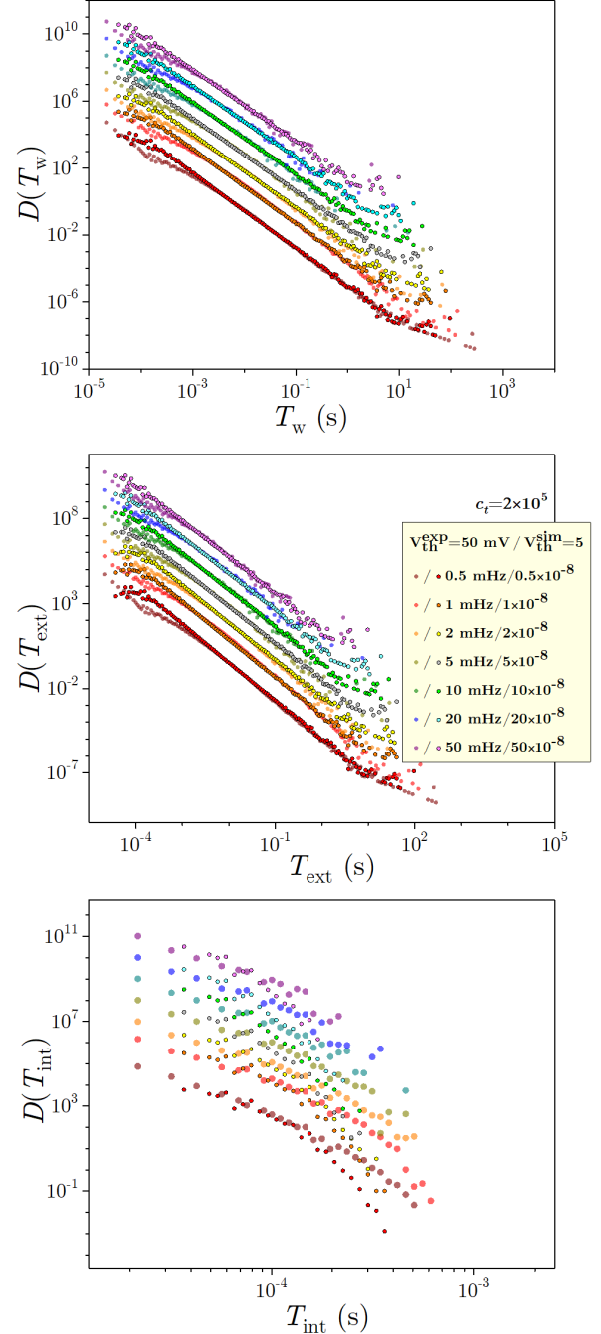


FIG. 11. Comparison of integrated distributions of total, external and internal waiting times, respectively, obtained in experiments and numerical simulations. The underlying data sets and all other parameters are the same as in Fig. 8.

which $M = 0$), one can see that the matching of data obtained from the experiments and numerical simulations is very good for $H < H_c$ and notably worse for $H > H_c$.

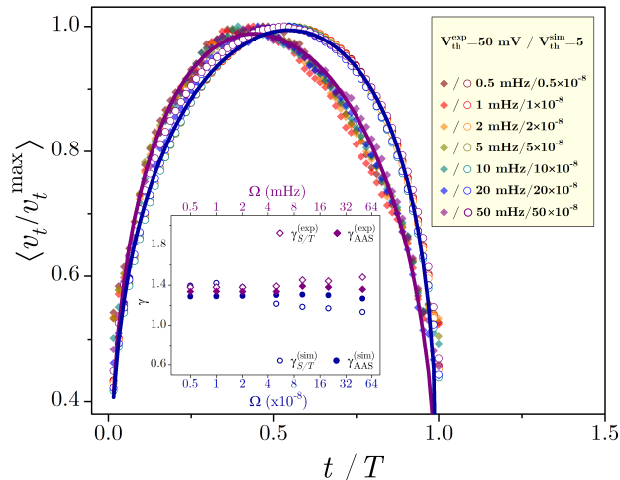


FIG. 12. Average avalanche shapes, shown by diamonds obtained from the experimental and by circles obtained from the simulational data. The graph shows against t/T (i.e. time t measured from the start of avalanche scaled by avalanche duration T) the values of $\langle v_t/v_t^{\max} \rangle$ (i.e. the average value of the response signal v_t scaled by its maximum value v_t^{\max} during the avalanche). The underlying data sets and all other parameters are the same as in Fig. 8. Full lines are fits to the functional form (10) and the inset shows the comparison of $\gamma_{S/T}$ to γ_{AAS} values for both simulations and experiment.

IV. DISCUSSION AND CONCLUSION

The main issue we faced in the comparison between the results obtained in our BN experiment and the possible results of the nonequilibrium athermal RFIM numerical simulations was the identification of the appropriate values of the RFIM parameters (lattice sizes, disorder R , and driving rate Ω) that would provide a reasonable matching of the two types of data.

To this end, we performed the simulations on the $32768 \times 2048 \times 8$ strip-like cubic lattice, the largest one we could use. This lattice with more than half a billion spins has approximately the same aspect ratio as the sample used in our experiment, which is important because the simulational results are affected by the lattice aspect ratio and also by the lattice finite size [54, 55, 57, 61]. These two facts prevented us to use a bigger lattice (e.g. doubled along each of its sides) because seeking the reasonable (R, Ω) pairs would be out of our reach due to the greatly increased running time of simulations at the corresponding computer memory demands.

Regarding the optimality of the value of disorder and the set of values of the driving rate in simulations for which the comparison with experimental findings is performed, we point out that these values depend on the choice of lattice (i.e. they might be somewhat different for another lattice due to the conformity of the finite-size and driving-rate scaling conditions [61]). Furthermore, even for the current choice of lattice, we do not claim

that these values are really optimal, but merely such that provide a reasonable matching of the experimental and (scaled) simulational data. This is in particular because the employed version of the RFIM is not indeed a realistic model for the Barkhausen noise which, instead of modeling the time evolution of magnetic domain pattern of driven disordered ferromagnetic samples responsible for the emission of BN, treats individual spins with the simplest mutual exchange coupling and the coupling with the quenched random magnetic field whose existence and characterization in real samples is still not well documented and understood. Nevertheless, as the employed RFIM version proved to be a paradigm for the description of the evolution of the nonequilibrium complex systems, we consider as valuable the comparison between its predictions and the characterization of the evolution recorded in the Barkhausen noise measurements.

To conclude, in this paper we compared the findings of the Barkhausen noise measurements and the simulations of the nonequilibrium athermal Random Field Ising Model (RFIM). The measurements were performed on a VITROPERM 800 metallic glass strip driven by the external magnetic field at the rates between 0.5 mHz and 50 mHz. All RFIM simulations were accomplished using suitable model parameters (lattice sizes with the aspect ratio as for the sample, a single value of disorder of the quenched random field, and a two-decade-wide range of driving). Applying these adjustments in simulations, allowed us to achieve a considerable matching with the experimental data. We hope that our findings will be helpful in the interpretation and analysis of experimental results obtained from a variety of strip-like disordered ferromagnetic samples driven at constant rates. Further on, the results of our study may also stimulate some future theoretical research, invoking the development of models that will more accurately capture the essence of the BN underlying dynamics.

ACKNOWLEDGMENTS

We acknowledge the support by the Ministry of Science, Technological Development and Innovation of Republic of Serbia (Agreements No. 451-03-47/2023-01/200162 and 451-03-47/2023-01/200122). LL acknowledges the support of the Research Council of Finland via the Academy Project BarFume (Project no. 338955). AD acknowledges the support of the Serbian Academy of Sciences and Arts via the Grant F133. We thank Dr. Tatjana Srećković from the Institute for Multidisciplinary Research, University of Belgrade, Serbia, for the thermal treatment of our samples, and Viktor Čosić from Custom Electronics d.o.o., Belgrade, Serbia, for his assistance in overcoming certain instruments malfunctions.

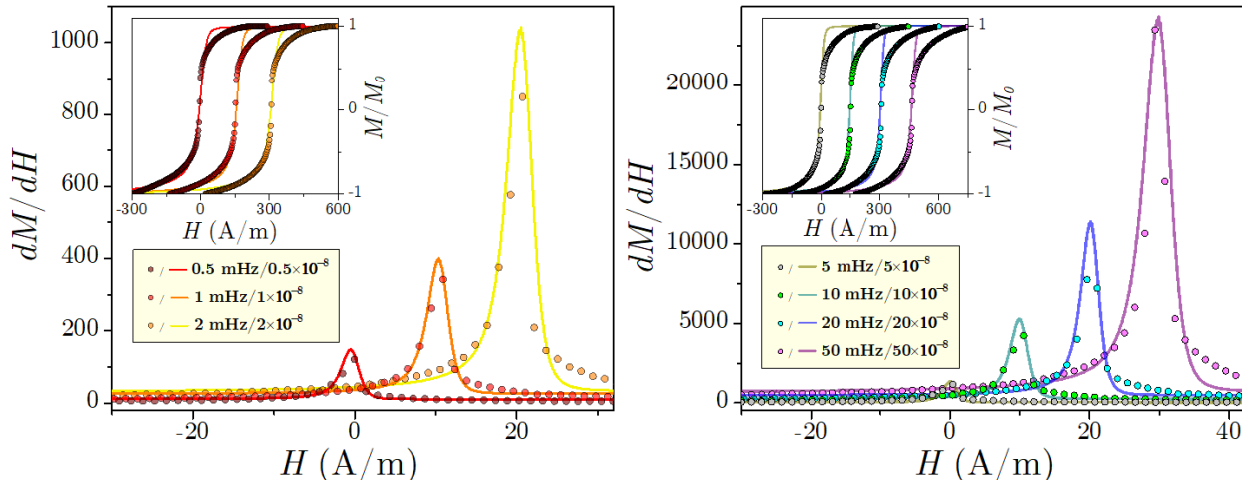


FIG. 13. Comparison of averaged magnetization and magnetic susceptibility curves obtained in experiments (symbols) and numerical simulations (full lines), the later scaled so as to achieve a matching with the experimental. The underlying data sets and other relevant parameters are the same as in Fig. 8. In the main panels, we show the magnetic susceptibilities dM/dH against the external magnetic field H , while in the insets we show M/M_0 (i.e. the magnetization M scaled by the saturation magnetization M_0) against H ; both types of curves correspond to the rising part of the hysteresis loop, and the dM/dH experimental curves are inverted (i.e. multiplied by -1), c.f. Fig. 2. In main panels/insets the curves are shifted for better visibility, namely susceptibilities/magnetizations in increments of $10 \text{ Am}^{-1}/150 \text{ Am}^{-1}$ relative to the (unshifted) curves which correspond to the $0.5 \text{ mHz}/5 \text{ mHz}$ driving rates in left/right panel.

REFERENCES

- [1] J. P. Sethna, K. A. Dahmen, and C. R. Myers, *Nature* **410**, 242-250 (2001)
- [2] H. Barkhausen, Zwei mit Hilfe der neuen Verstärker entdeckte Erscheinungen, *Physik Z.* **20**, 401 (1919)
- [3] B. Alessandro, C. Beatrice, G. Bertotti, and A. Montorsi, Domain-wall dynamics and Barkhausen effect in metallic ferromagnetic materials. II. Experiments, *J. Appl. Phys.* **68**, 2908-2915 (1990).
- [4] D. Spasojević, S. Bukvić, S. Milošević and H. E. Stanley, Barkhausen noise: Elementary signals, power laws, and scaling relations, *Phys. Rev. E* **54**, 2531 (1996)
- [5] M. Bahiana, B. Koiller, S. L. A. de Queiroz, J. C. Denardin, and R. L. Sommer, Domain size effects in Barkhausen noise, *Phys. Rev.* **59**, 3884-3887 (1999)
- [6] A. P. Mehta, A. C. Mills, K. A. Dahmen, and J. P. Sethna, Universal pulse shape scaling function and exponents: Critical test for avalanche models applied to Barkhausen noise, *Phys. Rev. E* **65**, 046139 (2002)
- [7] F. Colaiori, S. Zapperi, and G. Durin, Shape of a Barkhausen pulse, *J. Magn. Magn. Mater.* **272-276**, E533-E534 (2004)
- [8] G. Durin, and S. Zapperi, Scaling Exponents for Barkhausen Avalanches in Polycrystalline and Amorphous Ferromagnets, *Phys. Rev. Lett.* **84**, 4705-4708 (2000)
- [9] E. Puppini, Statistical Properties of Barkhausen Noise in Thin Fe Films, *Phys. Rev. Lett.* **84**, 5415-5418 (2000)
- [10] T. A. Moore, J. Rothman, Y. B. Xu, and J. A. C. Bland, Thickness-dependent dynamic hysteresis scaling behavior in epitaxial Fe/GaAs(001) and Fe/InAs(001) ultrathin films, *Jour. of App. Phys.* **89** 7018 (2001)
- [11] E. Puppini, E. Pinotti, and M. Brenna, Barkhausen noise in variable thickness amorphous finemet films, *J. Appl. Phys.* **101**, 063903 (2007)
- [12] D.-H. Kim, S.-B. Choe, and S.-C. Shin, Direct Observation of Barkhausen Avalanche in Co Thin Films, *Phys. Rev. Lett.* **90**, 087203 (2003)
- [13] K.-S. Ryu, H. Akinaga, and S.-C. Shin, Tunable scaling behaviour observed in Barkhausen criticality of a ferromagnetic film, *Nat. Phys.* **3**, 547-550 (2007)
- [14] S.-C. Shin, K.-S. Ryu, D.-H. Kim, S.-B. Choe, and H. Akinaga, Power-law scaling behavior in Barkhausen avalanches of ferromagnetic thin films, *J. Magn. Magn. Mater.* **310**, 2599-2603 (2007)
- [15] H.-S. Lee, K.-S. Ryu, K.-R. Jeon, S. S. P. Parkin, and S.-C. Shin, Breakdown of Barkhausen critical-scaling behavior with increasing domain-wall pinning in ferromagnetic films, *Phys. Rev. B* **83**, 060410 (2011)
- [16] F. Bohn, et al., Universal properties of magnetization dynamics in polycrystalline ferromagnetic films, *Phys. Rev.*

- E **88**, 032811 (2013)
- [17] F. Bohn, et al., Statistical properties of Barkhausen noise in amorphous ferromagnetic films, *Phys. Rev. E* **90**, 032821 (2014)
- [18] G. Durin, et al., Quantitative Scaling of Magnetic Avalanches, *Phys. Rev. Lett.* **117**, 087201 (2016)
- [19] F. Bohn, G. Durin, M. A. Correa, et al, Playing with universality classes of Barkhausen avalanches, *Sci. Rep.* **8**, 11294 (2018)
- [20] M. Honkanen, S. Santa-aho, L. Laurson, N. Eslahi, A. Foi, M. Vippola, Mimicking Barkhausen noise measurement by in-situ transmission electron microscopy - effect of microstructural steel features on Barkhausen noise, *Acta Materialia* **221**, 117378 (2021)
- [21] J. Uhl, S. Pathak, D. Schorlemmer et al., Universal Quake Statistics: From Compressed Nanocrystals to Earthquakes, *Sci. Rep.* **5**, 16493 (2015)
- [22] S. Santucci et al., Avalanches of imbibition fronts: Towards critical pinning, *Europhys. Lett.* **94**, 46005 (2011)
- [23] D. M. Dimiduk, C. Woodward, R. LeSar, and M. D. Uchic, Scale-Free Intermittent Flow in Crystal Plasticity, *Science* **312**, 1188 (2006)
- [24] P. D. Ispanovity, L. Laurson, M. Zaiser, I. Groma, S. Zapperi, and M. J. Alava Avalanches in 2D Dislocation Systems: Plastic Yielding Is Not Depinning, *Phys. Rev. Lett.* **112**, 235501 (2014).
- [25] S. Janičević, M. Ovaska, M. J. Alava, and L. Laurson, Avalanches in 2D dislocation systems without applied stresses, *J. Stat. Mech.* P07016, (2015)
- [26] P. D. Ispánovity, D. Ugi, G. Péterffy, et al. Dislocation avalanches are like earthquakes on the micron scale, *Nat. Commun.* **13**, 1975 (2022)
- [27] P. Ch. Ivanov et al., From $1/f$ noise to multifractal cascades in heartbeat dynamics, *Chaos: Interdisc. J. Nonlin. Sci.* **11**, 641 (2001)
- [28] C.-C. Lo et al., Dynamics of sleep-wake transitions during sleep, *Europhys. Lett.* **57**, 625 (2002)
- [29] N. Friedman, S. Ito, B. A. W. Brinkman, M. Shimono, R. E. L. DeVile, K. A. Dahmen, J. M. Beggs, and T. C. Butler, Universal Critical Dynamics in High Resolution Neuronal Avalanche Data, *Phys. Rev. Lett.* **108**, 208102 (2012)
- [30] S. R. Miller, S. Yu, and D. Plenz, The scale-invariant, temporal profile of neuronal avalanches in relation to cortical γ -oscillations, *Sci Rep* **9**, 16403 (2019); see also *Criticality in Neural Systems*, edited by D. Plenz and E. Niebur, Wiley Online Library (2014)
- [31] D. S. Fisher, Collective transport in random media: from superconductors to earthquakes, *Phys. Rep.* **301**, 113 (1998)
- [32] J. Davidsen and M. Baiesi, Self-similar aftershock rates, *Phys. Rev. E* **94**, 022314 (2016)
- [33] A. Bizzarri, A. Petri, A. Baldassarri, Earthquake dynamics constrained from laboratory experiments: new insights from granular materials, *Ann. Geophys.* **64**(4), SE 441 (2021)
- [34] J. Perelló, J. Masoliver, A. Kasprzak, and R. Kutner, Model for interevent times with long tails and multifractality in human communications: An application to financial trading, *Phys. Rev. E* **78**, 036108 (2008)
- [35] J. P. Bouchaud, Crises and Collective Socio-Economic Phenomena: Simple Models and Challenges, *J. Stat. Phys.* **151**, 567-606 (2013)
- [36] D. P. Belanger and T. Nattermann, *Spin Glasses and Random Fields* edited by Young A P World Scientific Singapore, pp. 251–298 (1998)
- [37] J. P. Sethna, K. A. Dahmen, S. Kartha, J. A. Krumhansl, B. W. Roberts and J. D. Shore, Hysteresis and hierarchies: Dynamics of disorder-driven first-order phase transformations, *Phys. Rev. Lett.* **70**, 3347 (1993)
- [38] O. Perković, K. A. Dahmen and J. P. Sethna, Disorder-induced critical phenomena in hysteresis: Numerical scaling in three and higher dimensions, *Phys. Rev. B* **59**, 6106 (1999)
- [39] J. P. Sethna, K. A. Dahmen and O. Perković, Random-field Ising models of hysteresis in *The Science of Hysteresis* edited by Bertotti G and Mayergoyz I Academic Press Amsterdam Vol. **2**, pp. 107-179 (2006)
- [40] T. Herranen and L. Laurson, Barkhausen noise from precessional domain wall motion, *Phys. Rev. Lett.* **122**, 117205 (2019)
- [41] S. Kaappa and L. Laurson, Barkhausen noise from formation of 360° domain walls in disordered permalloy thin films, *Phys. Rev. Research* **5**, L022006 (2023).
- [42] S. Zapperi, P. Cizeau, G. Durin, and H. E. Stanley, Dynamics of a ferromagnetic domain wall: Avalanches, depinning transition, and the Barkhausen effect, *Phys. Rev. B* **58**, 6353 (1998).
- [43] C. Frontera and E. Vives, Studying avalanches in the ground state of the two-dimensional random-field Ising model driven by an external field, *Phys. Rev. E* **62**, 7470 (2000)
- [44] Y. Liu and K. A. Dahmen, Unexpected universality in static and dynamic avalanches, *Phys. Rev. E* **79**, 061124 (2009)
- [45] Y. Liu and K. A. Dahmen, Random-field Ising model in and out of equilibrium, *Europhys. Lett.* **86**, 56003 (2009)
- [46] I. Balog, G. Tarjus, and M. Tissier, Criticality of the random field Ising model in and out of equilibrium: A non-perturbative functional renormalization group description, *Phys. Rev. B* **97**, 094204 (2018)
- [47] S. Bukvić and Dj. Spasojević, An alternative approach to spectrum baseline estimation, *Spectrochimica Acta Part B: Atomic Spectroscopy* **60**, 1308 (2005)
- [48] S. Bukvić, Dj. Spasojević, and V. Žigman Advanced fit technique for astrophysical spectra, *Astronomy & Astrophysics* **477**, 967 (2008)
- [49] L. Laurson, X. Illa, and M.J. Alava, The effect of thresholding on temporal avalanche statistics, *J. Stat. Mech.: Theo. Exp.*, P01019 (2009)
- [50] G. Durin G and S. Zapperi 2006 *The Science of Hysteresis*, edited by Bertotti, G. & Mayergoyz, I., Academic Press, Amsterdam **2** pp.181–267
- [51] It is known that the exponent value extracted through the linear fit applied in the scaling region can be significantly influenced by the presence of the cutoffs. More reliable exponent values are obtained by fitting the data to a suitably chosen model function reasonably describing the cutoffs, see e.g. in [69] the analytic form (15) describing the cutoff function.
- [52] D. Spasojević, S. Janičević and M. Knežević, Avalanche distributions in the two-dimensional nonequilibrium zero-temperature random field Ising model, *Phys. Rev. E* **84**, 051119 (2011)
- [53] D. Spasojević, S. Janičević and M. Knežević, Numerical Evidence for Critical Behavior of the Two-Dimensional Nonequilibrium Zero-Temperature Random Field Ising Model, *Phys. Rev. Lett.* **106** 175701 (2011)

- [54] D. Spasojević, S. Mijatović, V. Navas-Portela and E. Vives, Crossover from three-dimensional to two-dimensional systems in the nonequilibrium zero-temperature random-field Ising model, *Phys. Rev. E* **97**, 012109 (2018)
- [55] S. Mijatović, D. Jovković, S. Janičević, and D. Spasojević, Critical disorder and critical magnetic field of the nonequilibrium athermal random-field Ising model in thin systems, *Phys. Rev. E* **100**, 032113 (2019)
- [56] B. Tadić, S. Mijatović, S. Janičević, Dj. Spasojević and G. J. Rodgers, The critical Barkhausen avalanches in thin random-field ferromagnets with an open boundary, *Sci. Rep.* **9** 6349 (2019)
- [57] S. Mijatović, M. Branković, S. Graovac and D. Spasojević, Avalanche properties in striplike ferromagnetic systems, *Phys. Rev. E* **102**, 022124 (2020)
- [58] S. Janičević, D. Knežević, S. Mijatović and D. Spasojević, Scaling domains in the nonequilibrium athermal random field Ising model of finite systems, *J. Stat. Mech.*, 013202 (2021)
- [59] B. Tadić, Dynamic criticality in driven disordered systems: role of depinning and driving rate in Barkhausen noise, *Physica A* **270**, 125-134 (1999)
- [60] R. A. White and K. A. Dahmen, Driving Rate Effects on Crackling Noise, *Phys. Rev. Lett.* **91**, 085702 (2003)
- [61] S. Radić, S. Janičević, D. Jovković and D. Spasojević, The effect of finite driving rate on avalanche distributions, *J. Stat. Mech.* **2021** 093301 (2021)
- [62] D. Spasojević, and S. Janičević, Two-dimensional ferromagnetic systems with finite driving, *Chaos, Solitons and Fractals* **158**, 112033 (2022)
- [63] D. Spasojević, S. Radić, D. Jovković and S. Janičević, Spin activity correlations in driven disordered systems, *Journal of Stat.Mech.: Theory and Experiment*, 063302 (2022)
- [64] M. Kuntz, O. Perković, K. A. Dahmen, B. W. Roberts and J. P. Sethna, Hysteresis, avalanches, and noise, *Computing in Science Engineering* **1**, 73 (1999)
- [65] F. J. Pérez-Reche and E. Vives, Finite-size scaling analysis of the avalanches in the three-dimensional Gaussian random-field Ising model with metastable dynamics, *Phys. Rev. B* **67**, 134421 (2003)
- [66] F. J. Pérez-Reche and E. Vives, Spanning avalanches in the three-dimensional Gaussian random-field Ising model with metastable dynamics: Field dependence and geometrical properties, *Phys. Rev. B* **70**, 214422 (2004)
- [67] D. Spasojević, S. Janičević and M. Knežević, Analysis of spanning avalanches in the two-dimensional nonequilibrium zero-temperature random-field Ising model, *Phys. Rev. E* **89**, 012118 (2014)
- [68] M. C. Kuntz and J. P. Sethna, Noise in disordered systems: The power spectrum and dynamic exponents in avalanche models, *Phys. Rev. B* **62**, 11699–11708 (2000)
- [69] A. Rosso, P. Le Doussal, and K. J. Wiese, Avalanche-size distribution at the depinning transition: A numerical test of the theory, *Phys. Rev. B* **80**, 144204 (2009)
- [70] L. Laurson, X. Illa, S. Santucci, K. T. Tallakstad, K. J. Måløy, and M. J. Alava, Evolution of the average avalanche shape with the universality class, *Nat. Commun.* **4**, 2927 (2013)